Front. Energy 2025, 19(3): 382–394
https://doi.org/10.1007/s11708-025-1002-8

RESEARCH ARTICLE

Surface electron reconfiguration of ceric dioxide artificial interface layer by cationic doping for dendrite-free zinc anode

Linlong Lu[1,2], Zheng Wang[1,2], Jingwen Cai[1,2], Zhengyu Bao[1,2], Yukai Lan[1,2], Yinze Zuo (✉)[1,2], Yidong Jiang[1,2], Wei Yan (✉)[1,2], Jiujun Zhang (✉)[1,2]

1 Institute for New Energy Materials and Engineering, College of Materials Science and Engineering, Fuzhou University, Fuzhou 350108, China
2 Fujian Engineering Research Center of High Energy Batteries and New Energy Equipment and Systems, Fuzhou University, Fuzhou 350108, China

Abstract Aqueous zinc metal batteries (ZMBs) are regarded as strong contenders in secondary battery systems due to their high safety and abundant resources. However, the cycling performance of the Zn anode and the overall performance of the cells have often been hindered by the formation of Zn dendrites and the occurrence of parasitic side reactions. In this paper, a surface electron reconfiguration strategy is proposed to optimize the adsorption energy and migration energy of Zn^{2+} for a better Zn^{2+} deposition/stripping process by adjusting the electronic structure of ceric dioxide (CeO_2) artificial interface layer with copper atoms (Cu) doped. Both experimental results and theoretical calculations demonstrate that the $Cu_2Ce_7O_x$ interface facilitates rapid transport of Zn^{2+} due to the optimized electronic structure and appropriate electron density, leading to a highly reversible and stable Zn anode. Consequently, the $Cu_2Ce_7O_x$@Zn symmetric cell exhibits an overpotential of only 24 mV after stable cycling for over 1600 h at a current density of 1 mA/cm^2 and a capacity of 1 mAh/cm^2. Additionally, the cycle life of Cu/Zn asymmetric cells exceeds 2500 h, with an average Coulombic efficiency of 99.9%. This paper provides a novel approach to the artificial interface layer strategy, offering new insights for improving the performance of ZMBs.

Keywords Zn metal batteries, interface layer, solvation structure, electronic structure, $Cu_2Ce_7O_x$

1 Introduction

In the context of global energy structure transformation, the utilization and storage of renewable energy have become key scientific and technological issues [1–3]. Among various energy storage technologies, aqueous Zn metal batteries (ZMBs) have garnered significant attention due to their advantages, including safety, environmental friendliness, low cost, and abundant resources [4–7]. However, further application of ZMBs is hindered by several issues, such as the formation of Zn dendrite [8–12], side-reactions, and corrosion of Zn anode [13–15], which are primarily caused by the sluggish kinetics of Zn^{2+} desolvation [16,17]. Therefore, optimizing the solvation shell of $[Zn(H_2O)_6]^{2+}$ to accelerate the Zn^{2+} desolvation process is crucial for addressing the challenges faced by ZMBs [18–21].

Several strategies have been explored to accelerate the Zn^{2+} desolvation process: 1) Electrolyte optimization: Certain electrolytes can provide more hydrogen bond donors and acceptors [22–24], or have a higher affinity for Zn^{2+}. These electrolytes interact with Zn^{2+} preferentially and enter its solvation shell, altering the solvation structure environment. For example, DMSO can occupy more positions in the solvation structure of Zn^{2+} and reduce direct contact between H_2O molecules and Zn^{2+}, due to the high number of hydrogen bond donors of dimethyl sulfoxide [25] (DMSO) compared to H_2O. However, electrolyte additives may spontaneously precipitate during cell operation [26,27], thereby potentially blocking ion transport channels. 2) Structural

Received Jan. 3, 2025; accepted Mar. 6, 2025; online Apr. 5, 2025
Correspondences: Yinze Zuo, yinzezuo@fzu.edu.cn;
Wei Yan, weiyan@fzu.edu.cn;
Jiujun Zhang, jiujun.zhang@fzu.edu.cn

design: The design of three-dimensional (3D) anodes [28,29] with abundant pores can provide more contact sites for solvent molecules and Zn^{2+}, facilitating better Zn^{2+} diffusion. For example, fibrous Zn anodes [30] prepared using techniques such as electrospinning are intertwined with each other to form a 3D network structure. This structure [31] can shorten the diffusion path for Zn^{2+} and provide additional sites for solvation. However, the uneven distribution of current density in such structures, and the uneven deposition of desolvated Zn^{2+} may negatively affect the performance of the cell. 3) Surface modification: Interface layers [32–34] that strongly interact with Zn^{2+} can facilitate the shedding of surrounding solvent molecules, reducing the nucleation energy barrier and accelerating the transmission of Zn^{2+} [35,36]. For example, Cao's group [37] used a $BaTiO_3$/P(VDF-TrFE) (BTO/PVT) interface layer to reduce the nucleation overpotential and charge transfer resistance (R_{ct}). Zhou's group [32] proposed the use of *in situ*-grown polyaniline to improve the redox kinetics of Zn^{2+} and redox kinetics. A zincophilic interface layer with strong chemical adsorption Zn^{2+} [38–41], can improve the electrochemical performance of Zn anodes. Although enhancing the adsorption capacity for Zn^{2+} can reduce the nucleation overpotential and guide the uniform deposition of Zn^{2+} [42], excessive adsorption can hinder the migration of Zn^{2+} near the interface, the transfer of Zn^{2+} on the anode surface, negatively impacting the overall performance of the cell. The weak adsorption effect of the non-zincophilic interface layer on Zn^{2+} is often accompanied by a lower migration energy barrier, which can achieve rapid transfer of Zn^{2+} and a lower overpotential. However, it also leads to Zn^{2+} being too easy to move on the surface, hindering the uniform deposition of Zn^{2+}. Therefore, the interlayer is equally important for the adsorption and migration of Zn^{2+} [43–45].

In this work, Cu atoms were successfully doped into Ce atoms to form $Cu_2Ce_7O_x$ through a simple high-temperature calcination process [46]. Compared to ceric dioxide (CeO_2), the electron density near the Ce atoms in $Cu_2Ce_7O_x$ decreases, and electrons become more dispersed between Cu and O atoms (Fig. 1(a)). Moreover, $Cu_2Ce_7O_x$ generates an unusual s-p-d orbital hybridization, which triggers electron rearrangement. This alters the electrostatic force due to the alteration of the electron cloud distribution, enhancing the interaction between the O atoms in Ce-O and Zn, thereby improving the chemical

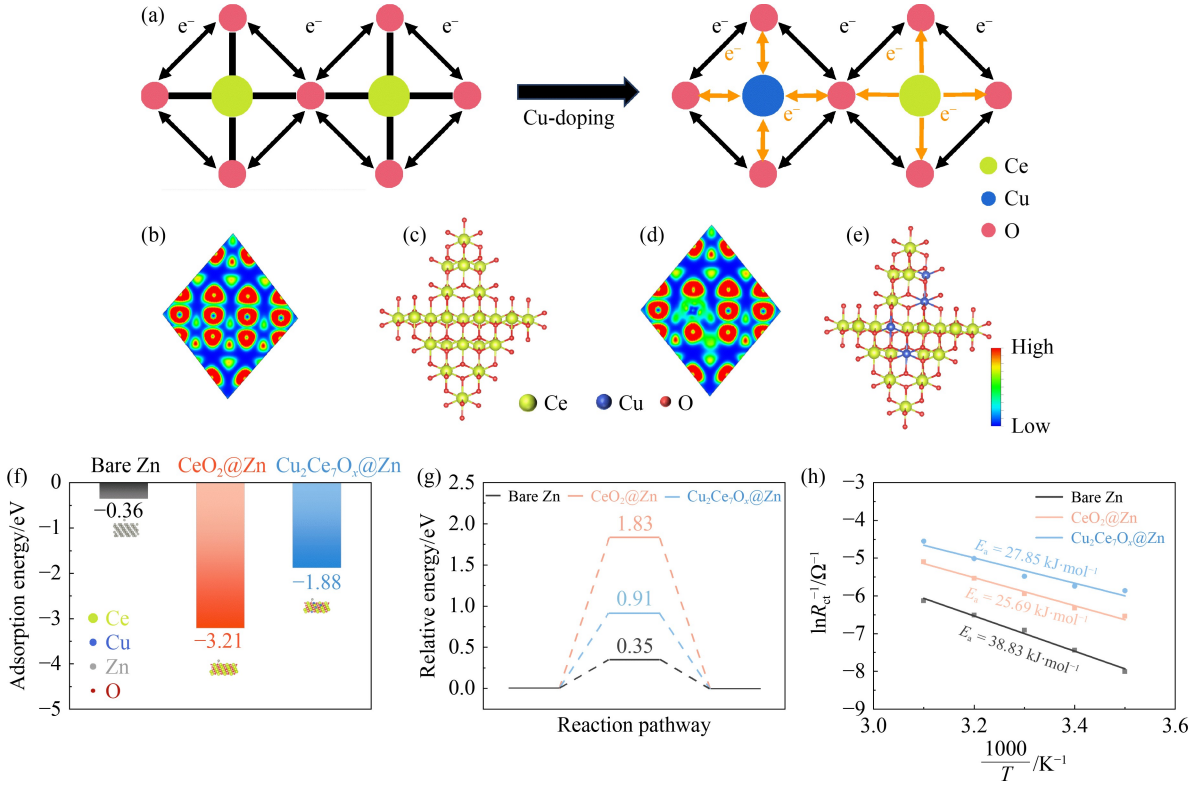

Fig. 1 Structure regulation of CeO_2 doped with Cu and the electrochemical performance of Zn^{2+}.

(a) Electron transfer for Cu atoms doping CeO_2 (green spheres: Ce atoms, blue spheres: Cu atoms, red spheres: O atoms.); (b, c) crystal structure and ELF of CeO_2; (d, e) crystal structure and ELF of $Cu_2Ce_7O_x$; (f) adsorption energies of bare Zn, CeO_2, and $Cu_2Ce_7O_x$ for Zn^{2+} ions; (g) Zn^{2+} ions migration energy barriers on bare Zn, CeO_2@Zn and $Cu_2Ce_7O_x$@Zn surface; (h) activation energies of symmetric cells with bare Zn, CeO_2@Zn and $Cu_2Ce_7O_x$@Zn electrode.

affinity for Zn^{2+}. Since $Cu_2Ce_7O_x$, as the Zn anode interface layer, has appropriate adsorption energy and migration energy, it not only improves the cycling ability of the Zn anode but also reduces the nucleation overpotential during the deposition and dissolution processes.

The $Cu_2Ce_7O_x$@Zn/$Cu_2Ce_7O_x$@Zn symmetric cell exhibits a low overpotential of 24 mV, with stable cycling for over 1600 h at a current density of 1 mA/cm^2 and an electrical capacity of 1 mAh/cm^2, which is more than 10 times that of a bare Zn anode. The Cu/$Cu_2Ce_7O_x$@Zn/Cu asymmetric cells show a long cycle life of over 2500 h, with an average Coulombic efficiency of 99.9%. Furthermore, when assembled into a $Cu_2Ce_7O_x$@Zn/MnO_2 full cell, the battery maintains an excellent capacity retention of 88.9% over the first 800 cycles at 1 A/g. This work offers a novel strategy for constructing stable ZMBs, providing a significant step forward in their development for energy storage applications.

2 Results and discussion

The zincophilic interface layer constructed at the electrode/electrolyte interface of a Zn anode plays a significant role in promoting the desolubilization of $[Zn(H_2O)_6]^{2+}$ and ensuring the even deposition of Zn^{2+} ions [47,48]. To explore the mechanism of CeO_2 and $Cu_2Ce_7O_x$ on interfacial solvation, the electron distribution in these materials was analyzed using theoretical calculation. The electron localization function (ELF) was used to analyze the distribution of electrons around atoms. As shown in Figs. 1(b)–1(e), doping Cu atoms to replace a portion of the Ce atoms in CeO_2 results in an unusual s-p-d orbital hybridization, which induces electron rearrangement, thereby enhancing the Ce-O bond. This doping of Cu atoms causes the electrons around Ce and O atoms to disperse. The decrease in electron density near O atoms weakens the chemical interaction between O atoms and Zn^{2+}, which reduces the chemical affinity of O atoms for Zn^{2+}. The behavior of Zn^{2+} at the electrode/electrolyte interface was verified by calculating the adsorption energy, migration energy for Zn^{2+} and the activation energy.

To further investigate the behavior of Zn^{2+} at the electrode/electrolyte interface, the adsorption energy, migration energy, and activation energy were calculated. The adsorption energies of CeO_2 and $Cu_2Ce_7O_x$ for Zn^{2+} were calculated to evaluate the chemical affinity of the interface layer to Zn^{2+}. The adsorption energy of the CeO_2 interface layer for Zn^{2+} was found to be −3.21 eV, which is significantly higher than that of bare Zn (−0.36 eV), suggesting a reduction in the dissolution energy barrier (Fig. 1(f)). However, excessive adsorption energy can hinder the subsequent Zn^{2+} migration and nucleation and may cause deactivation of the CeO_2 interface layer, which is harmful to the construction of highly stable ZMBs. In contrast, $Cu_2Ce_7O_x$ exhibits a moderate adsorption energy of −1.88 eV, which is ideal for reducing the dissolution energy barrier while ensuring long-term ZMBs operation.

Additionally, the migration energy of Zn^{2+} was assessed. As shown in Fig. 1(g), on the bare Zn surface, the migration energy of Zn^{2+} is 0.35 eV, which is beneficial to two-dimensional (2D) planar diffusion of Zn^{2+}. Moreover, on the $Cu_2Ce_7O_x$ interface layer, the migration energy increases to 0.91 eV, which can inhibit excessive 2D planar diffusion, promoting more uniform Zn^{2+} deposition. However, the migration energy on the CeO_2 interface layer is 1.83 eV, likely due to its high adsorption energy, which is not conducive to Zn^{2+} migration and nucleation. Moreover, the activation energy for the reaction kinetics was calculated by measuring the charge transfer resistance (R_{ct}) to reaction kinetics (Fig. S1). The activation energy of the $Cu_2Ce_7O_x$@Zn electrode was found to be 27.85 kJ/mol, which is lower than that of the bare Zn electrode (38.83 kJ/mol), indicating fast reaction kinetics on the $Cu_2Ce_7O_x$@Zn surface (Fig. 1(h)).

These findings suggest that the $Cu_2Ce_7O_x$ interface layer optimally balances adsorption and migration energy for Zn^{2+}, improving the performance of Zn metal anodes in aqueous zinc metal batteries (ZMBs) by enhancing both the dissolution and deposition processes.

To confirm the successful doping of Cu atoms into CeO_2, a series of characterizations were conducted on the synthesized materials. As shown in Fig. 2(a) with X-ray diffraction (XRD analysis), the diffraction peaks at 28.6°, 33.1°, 47.5°, and 56.3° correspond to the (111), (200), (220), and (311) crystal planes of CeO_2, respectively, based on the JCPDS-43-1002 reference. When compared to pure CeO_2, due to the change of the lattice of CeO_2 by Cu doping, the XRD characteristic peak for $Cu_2Ce_7O_x$ shift toward lower energy levels, showing that Cu doping has altered the lattice structure of CeO_2. These XRD results suggest that Cu atoms are incorporated into the crystal structure of CeO_2, replacing some Ce atoms.

SEM and high-resolution TEM images show that $Cu_2Ce_7O_x$ is in a nanosheet-like morphology (Fig. 2(b)). Moreover, elemental analysis based on the mass ratio of Cu and Ce indicates the presence of 8.34% Cu and 27.97% Ce, respectively, which approximates a 2:7 ratio. Energy dispersive X-ray spectroscopy (EDS) (Fig. S2) further confirms that Cu, Ce, and O are uniformly distributed throughout $Cu_2Ce_7O_x$, providing additional evidence that Cu atoms have been successfully doped into the CeO_2 matrix.

In the TEM analysis, the (111) crystal plane of CeO_2 was detected and measured, with a lattice spacing of 0.322 nm for $Cu_2Ce_7O_x$ (Fig. 2(c)). This value is larger than that of pure CeO_2 (Fig. S3), suggesting that Cu atom

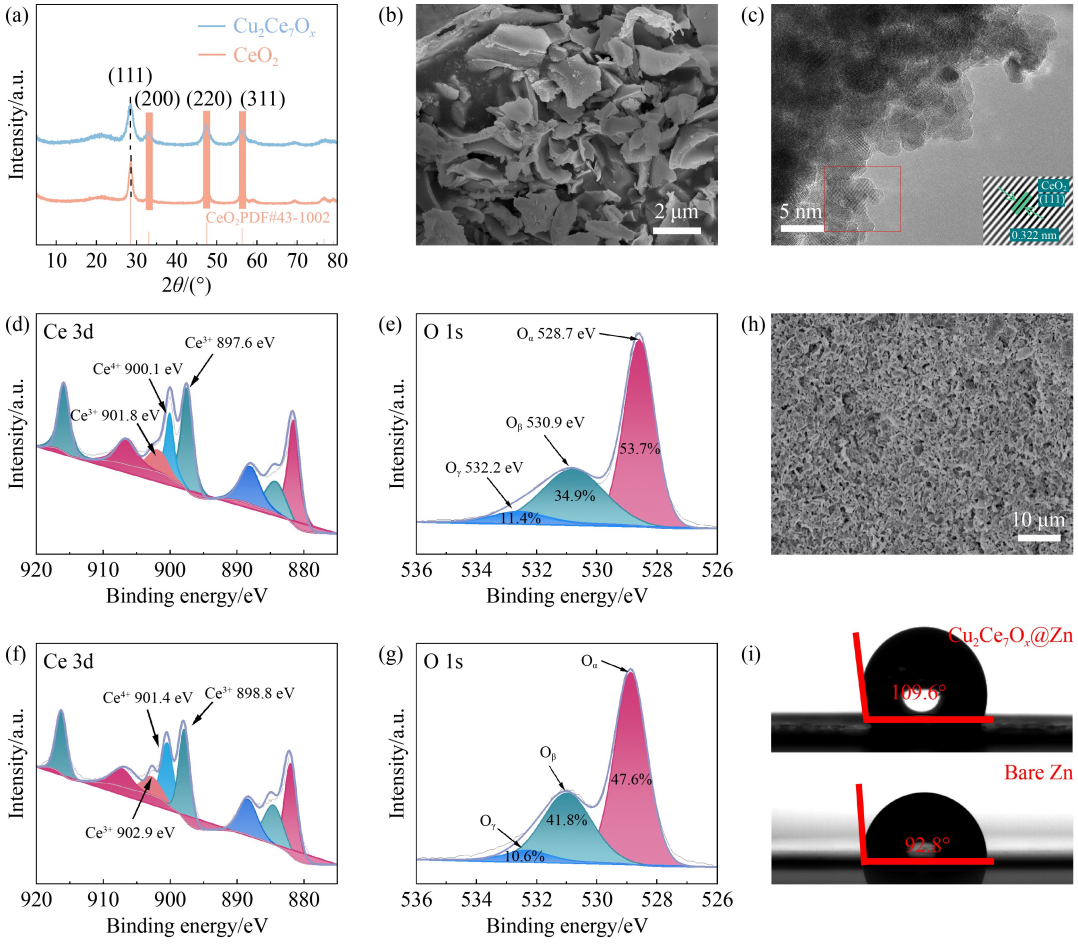

Fig. 2 Structural characterization of $Cu_2Ce_7O_x$ and impact on the surface properties of Zn electrodes.

(a) XRD patterns of $Cu_2Ce_7O_x$ and CeO_2; (b) Scanning electron microscopy (SEM); (c) transmission electron microscope (TEM) images of $Cu_2Ce_7O_x$; (d) XPS spectra of Ce 3d of CeO_2; (e) XPS spectra of O 1s of CeO_2; (f) XPS spectra of Ce 3d of $Cu_2Ce_7O_x$; (g) XPS spectra of O 1s of $Cu_2Ce_7O_x$; (h) SEM image of $Cu_2Ce_7O_x$@Zn surface; (i) contact angle tests on bare Zn and $Cu_2Ce_7O_x$@Zn with $ZnSO_4$ electrolyte.

doping has expanded the lattice structure of CeO_2. According to the Bragg's equation, the shift in the XRD peaks toward lower angles is consistent with an increase in lattice spacing, which further confirms that the doping of Cu atoms into CeO_2 causes a lattice distortion. Notably, the lattice spacing corresponding to Cu atoms was not detected in the TEM, indicating that Cu atoms are fully integrated into the CeO_2 substrate.

X-ray photoelectron spectroscopy (XPS) was also employed to examine the chemical state of CeO_2 and $Cu_2Ce_7O_x$ [49]. The Ce 3d spectrum revealed two distinct peaks for Ce^{3+} and Ce^{4+} in both CeO_2 and $Cu_2Ce_7O_x$. In the case of CeO_2, the binding energies of Ce^{3+} and Ce^{4+} for the $Cu_2Ce_7O_x$ are higher than those of CeO_2. Additionally, the intensity of the Ce^{4+} peak at 901.4 eV in the $Cu_2Ce_7O_x$ is higher than in CeO_2, while the intensity of the nearby Ce^{3+} peak is diminished (Figs. 2(d) and 2(f)). This observation shows that the doped Cu atoms reduce the electron density around Ce atoms.

The O 1s XPS spectrum of CeO_2 and $Cu_2Ce_7O_x$ shows three distinct oxygen peaks: O_α, O_β, and O_γ at 528.7, 530.9, and 532.2 eV, corresponding to oxygen atoms in the lattice structure, oxygen vacancy in the materials, and adsorbed oxygen species, respectively. It is worth noting that the proportion of oxygen vacancies (O_β) in $Cu_2Ce_7O_x$ has increased compared to CeO_2, which further modifies the electronic structure of $Cu_2Ce_7O_x$, promoting $Cu_2Ce_7O_x$ surface electron rearrangement (Figs. 2(e) and 2(g)).

The $Cu_2Ce_7O_x$ material was then uniformly coated on a Zn foil using a simple doctor blade interface layer process, forming a 300 nm thick interface layer (Figs. S5 and S6). SEM images reveal that the nanosheet-like structure of $Cu_2Ce_7O_x$ is still retained (Fig. 2(h)), and the $Cu_2Ce_7O_x$ interface layer remains smooth and dense, which is beneficial in reducing material shedding due to volume changes on the surface during cycling.

To investigate the interaction between $Cu_2Ce_7O_x$ and the electrolyte, the contact angle of electrolyte on bare Zn and $Cu_2Ce_7O_x$@Zn in a 2 mol/L $ZnSO_4$ solution

was measured. The contact angles for bare Zn and $Cu_2Ce_7O_x$@Zn were found to be 92.8° and 109.6°, respectively (Fig. 2(i)). The higher contact angle of $Cu_2Ce_7O_x$@Zn demonstrate better hydrophobicity compared to bare Zn, which can reduce the access of H_2O molecules to the electrode/electrolyte interface, thereby improving the overall performance of the Zn anode in zinc metal batteries.

In summary, these characterizations confirm that Cu atoms have been successfully doped into CeO_2, and the resulting $Cu_2Ce_7O_x$ material exhibits significant changes in its crystal structure, electronic properties, and interaction with the electrolyte, all of which contribute to enhanced performance in zinc metal batteries.

The electrode/electrolyte interface plays a crucial role in determining the stability and performance of zinc metal batteries (ZMBs). In aqueous ZMBs, the stability of the Zn anode is even more crucial. Therefore, it is essential to conduct a series of analyses of the electrode/electrolyte interface to understand the impact of the interface on cell performance. One key factor influencing this is the solvation structure of Zn^{2+} ions, which can exist in several ion pair forms [50]: solvent-separated ion pair (SSIP), contact ion pair (CIP), and aggregate ion pair (AGG). Raman spectroscopy can effectively detect SSIP and CIP, and it can be used to evaluate the interfacial desolvation kinetics of Zn^{2+} ions based on the relative ratio of these ion pairs (Fig. 3(a)).

Raman spectroscopy [51,52] was used to investigate the interfacial solvation structure on bare Zn/electrolyte, CeO_2@Zn/electrolyte, and $Cu_2Ce_7O_x$@Zn/electrolyte interfaces. The results reveal that the proportion of CIP on $Cu_2Ce_7O_x$@Zn is 58.4%, which is higher than that on CeO_2@Zn (48.9%) and bare Zn (42.4%). This indicates that more SO_4^{2-} participate in the solvation structure and bound H_2O content is reduced. A higher proportion of CIP can promote the desolvation of $[Zn(H_2O)_6]^{2+}$ and reduce the adsorption and decomposition of H_2O molecules at the interface, improving the overall performance (Fig. 3(b)).

To further explore the solvation structure of the $ZnSO_4$ electrolyte at the electrode/electrolyte interface, Fourier transform infrared spectroscopy (FTIR) was used to analyze the interactions between three kinds of Zn electrode [53,54]. In the FTIR spectra, characteristic peaks at 1025–1210, 1600–1800, and 3200–3700 cm^{-1} corresponded to the interactions of Zn^{2+} with SO_4^{2-}, and the O–H bond in H_2O molecules, and hydrogen bonds, respectively (Figs. 3(c)–3(e) and S7). Compared to the blank electrolyte, the characteristic peak of SO_4^{2-} in $ZnSO_4$ electrolyte on the $Cu_2Ce_7O_x$ surface exhibits a redshift, indicating that SO_4^{2-} participates more actively in the solvation structure. This increases the proportion of CIP and decreases the desolvation energy barrier. Additionally, the O–H bond of H_2O molecules in $ZnSO_4$ electrolyte on the $Cu_2Ce_7O_x$ surface undergoes a blueshift, indicating that $Cu_2Ce_7O_x$ weakens the interaction between H_2O molecules, thereby increasing the proportion of free H_2O. The peak for hydrogen bonding undergoes a redshift, indicating that $Cu_2Ce_7O_x$ enhances the hydrogen bond network [55] and increases the stability of the electrolyte.

To quantify the influence of artificial interface on the solvation structure, the desolvation energy required for the transition from $[Zn(H_2O)_6]^{2+}$ to Zn^{2+} was calculated (Figs. 3(f) and S9). The results show that $Cu_2Ce_7O_x$@Zn/electrolyte interface has lower desolvation energy due to the enhanced hydrogen bond network, which reduces the binding energy between H_2O molecules and Zn^{2+} in $[Zn(H_2O)_6]^{2+}$, thereby accelerating the redox reaction kinetics.

Molecular dynamics (MD) simulations were employed to further investigate the solvation structure at the electrode/electrolyte interface. On the CeO_2@Zn interface, Zn^{2+} is strongly adsorbed to the interior of CeO_2, resulting in the loss of interaction between Zn^{2+} and SO_4^{2-} (Fig. S8). MD simulations also provided the proportions on SSIP, CIP, and AGG for the $ZnSO_4$ electrolyte on bare Zn, CeO_2@Zn, and $Cu_2Ce_7O_x$@Zn interfaces (Fig. 3(g)). The proportion of CIP near the $Cu_2Ce_7O_x$@Zn interface is the highest, reaching 40%, which is higher than that of CeO_2@Zn (38%) and bare Zn (27%). This observation is consistent with the results from MD simulations, FTIR, and Raman spectroscopy.

Moreover, to investigate the stability of these interfaces, MD simulations were also used to calculate the content of interfacial free H_2O (Fig. 3(h)). The content of free H_2O near the bare Zn interface is 84.6%, which is relatively low and could hinder the Zn^{2+} desolvation process. In contrast, the interfaces of $Cu_2Ce_7O_x$@Zn (86.3%) and CeO_2@Zn (86.5%) have a higher content of free H_2O, indicating that these interfaces enhance the desolvation process of Zn^{2+}.

Finally, the radial distribution function (RDF) and coordination number of Zn^{2+} with H_2O molecules and SO_4^{2-} at these interfaces were also calculated using MD simulations (Figs. 3(i) and 3(j)). The coordination number [21] for Zn-O (SO_4^{2-}) of $ZnSO_4$ electrolyte at the $Cu_2Ce_7O_x$ interface is 0.61, which is higher than that at the CeO_2 (0.23) and bare Zn interfaces (0.50). In particular, the coordination number of Zn-O (SO_4^{2-}) of $ZnSO_4$ electrolyte on CeO_2 interface is 0.23, which is lower than that on the $Cu_2Ce_7O_x$ interface and the bare Zn interface due to the excessive adsorption of CeO_2 for Zn^{2+}.

In conclusion, this analysis demonstrates that an appropriate adsorption capacity for Zn^{2+} is crucial for enhancing the desolvation process and improving the redox kinetics of Zn^{2+}, ultimately contributing to the improved performance of ZMBs.

To demonstrate the protective effect of the $Cu_2Ce_7O_x$ interlayer for Zn anode, as well as its role in inhibiting

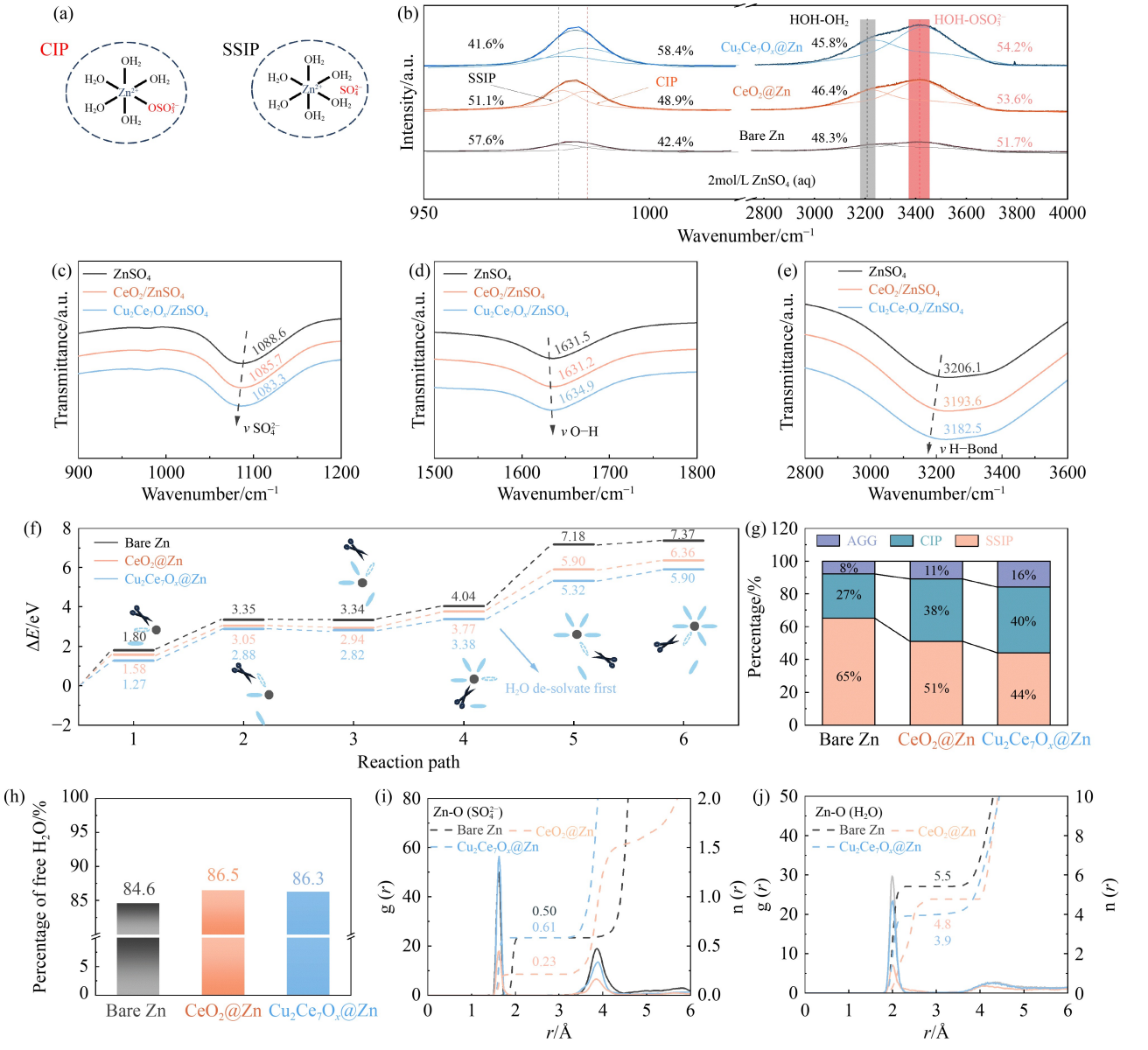

Fig. 3 Electrochemical characterization of Zn^{2+} solvation structures and theoretical calculations.

(a) Structure of CIP and SSIP of $[Zn(H_2O)_6]^{2+}$ in $ZnSO_4$ electrolyte; (b) Raman spectroscopy of bare Zn/electrolyte, CeO_2@Zn/electrolyte, and $Cu_2Ce_7O_x$@Zn/electrolyte interfaces; (c, d, e) FTIR of bare Zn/electrolyte, CeO_2@Zn/electrolyte, and $Cu_2Ce_7O_x$@Zn/electrolyte interfaces; (f) desolvation energy barriers of bare Zn, CeO_2@Zn, and $Cu_2Ce_7O_x$@Zn; (g) proportions of AGG, CIP, and SSIP near the interface of bare Zn, CeO_2@Zn, and $Cu_2Ce_7O_x$@Zn obtained by MD simulations; (h) content of free H_2O near the interface of bare Zn, CeO_2@Zn, and $Cu_2Ce_7O_x$@Zn; (i, j) RDF of H_2O and SO_4^{2-} of solvation structure on bare Zn, CeO_2@Zn, and $Cu_2Ce_7O_x$@Zn interface layer.

side reactions and promoting uniform deposition of Zn^{2+}, the immersion experiment of the anode without or with the $Cu_2Ce_7O_x$@Zn interface was performed, respectively (Figs. 4(a) and 4(b)). After soaking for seven days, the bare Zn surface showed the formation of flake-like $Zn_4SO_4(OH)_6{\cdot}3H_2O$ (ZHS), a product of the corrosion process. Nevertheless, thanks to the protective effect of the $Cu_2Ce_7O_x$ artificial interface layer, no significant formation of ZHS was observed on the $Cu_2Ce_7O_x$@Zn surface (Figs. 4(c), 4(d) and S10), indicating that the $Cu_2Ce_7O_x$ interlayer has an excellent anti-corrosion ability. This protective layer prevents the anode interface from being eroded by H_2O molecule, hereby inhibiting the generation of ZHS.

To understand the impact of $Cu_2Ce_7O_x$ on the Zn deposition behavior, *in situ* optical microscopic was performed on the electrode without or with $Cu_2Ce_7O_x$ interface in $ZnSO_4$ electrolyte at a current density of 5 mA/cm^2 (Figs. 4(e) and 4(f)). After 10 min of deposition, protrusions began to form on the surface of

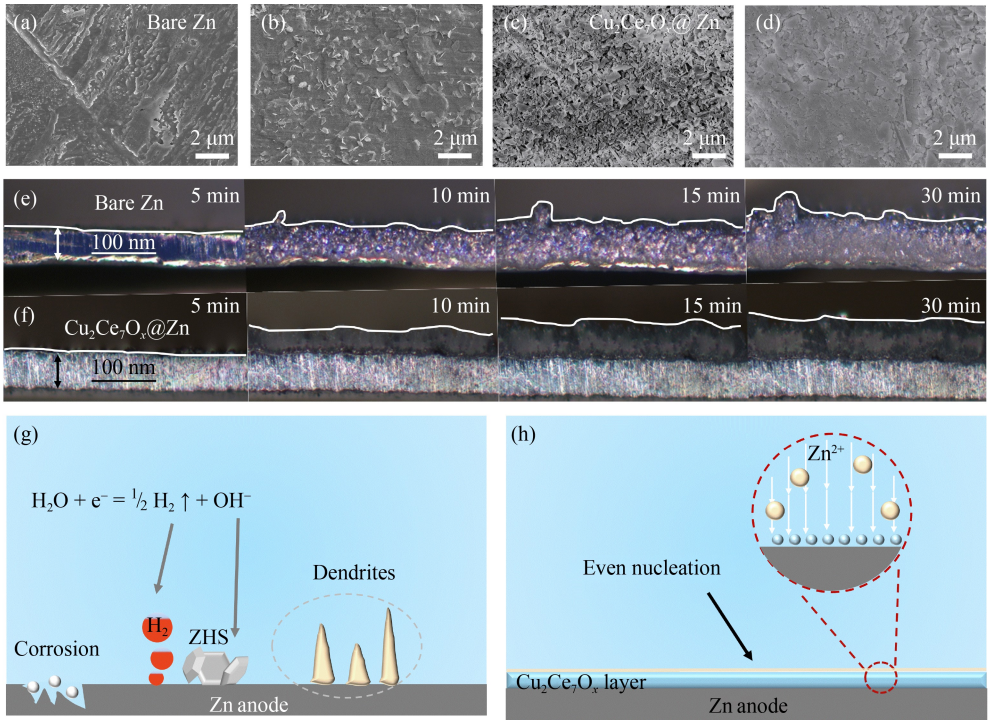

Fig. 4 Corrosion resistance and dendrite-free growth and mechanism diagram.

(a, b) Microstructures of bare Zn in the initial state and after soaking for seven days; (c, d) SEM images of $Cu_2Ce_7O_x$@Zn in the initial state and finial state of seven days soaking in 2 mol/L $ZnSO_4$ electrolyte; *in situ* optical microscope images of (e) bare Zn and (f) $Cu_2Ce_7O_x$@Zn electrodes after deposition for different times at the current density 5 mA/cm^2; (g) interfacial reaction process without artificial interface; (h) interfacial reaction process with $Cu_2Ce_7O_x$@Zn artificial interface.

the bare Zn electrode. As time increased to 30 min, these protrusions grow in size, causing the bare Zn surface to become very uneven. These protrusions would eventually continue to grow under the action of an electric field and finally form dendrites. In contrast, after 30 min of deposition under the same current conditions, the $Cu_2Ce_7O_x$@Zn surface remained flat with no protrusions, demonstrating the protective effect of the $Cu_2Ce_7O_x$ interface layer on Zn electrode.

Further tests using a symmetric cell with bare Zn electrode or $Cu_2Ce_7O_x$@Zn electrode after several cycles were conducted and analyzed by SEM (Fig. S11). After 20 cycles, the bare Zn surface exhibited visible ZHS, indicating uneven Zn deposition. After 50 cycles, the bare Zn surface began to crack due to volume changes caused by uneven deposition and stripping, as well as dendrite growth. In contrast, no obvious ZHS were observed on the $Cu_2Ce_7O_x$@Zn surface, where Zn^{2+} was evenly deposited on the $Cu_2Ce_7O_x$@Zn electrode surface in a sheet-like form after 50 cycles, indicating stable and uniform deposition behavior on the $Cu_2Ce_7O_x$@Zn electrode.

In conclusion, the $Cu_2Ce_7O_x$ interlayer effectively promotes the smooth and uniform deposition of Zn^{2+} on the anode surface. The schematic diagram of the mechanism (Figs. 4(g) and 4(h)) shows that the $Cu_2Ce_7O_x$@Zn interlayer inhibits the formation of ZHS and inhibits the hydrogen evolution reaction (HER) [56,57], which enable Zn^{2+} to be uniformly deposited on the anode surface, inhibiting the appearance of Zn dendrites. This ultimately enhances the stability and lifespan of the Zn anode in zinc metal batteries.

To evaluate the impact of $Cu_2Ce_7O_x$ on regulating the Zn deposition behavior and overall cell performance, symmetric cells with different electrode configurations, i.e., bare Zn/bare Zn, CeO_2@Zn/CeO_2@Zn, and $Cu_2Ce_7O_x$@Zn/$Cu_2Ce_7O_x$@Zn, were assembled and subjected to a series of electrochemical tests.

Nucleation behavior: At an overpotential of −150 mV, chronoamperometry was performed to analyze the respective nucleation modes for nucleation modes (Fig. 5(a)). The current density of the bare Zn keeps increasing for up to 300 s, a behavior attributed to preferential nucleation occurring in local regions on the electrode surface. Zn^{2+} preferentially accumulates in these regions for nucleation, causing the local current density to increase continuously, indicative of an irregular 2D deposition nucleation mode. This irregular nucleation causes Zn^{2+} to easily move freely on the anode surface, when it reaches the Zn anode surface. Moreover, the Zn^{2+} will continuously deposit randomly in places with lower nucleation energy, eventually leading to a homogeneous surface of the Zn anode which is prone to dendrite formation. In contrast, the symmetric cells with

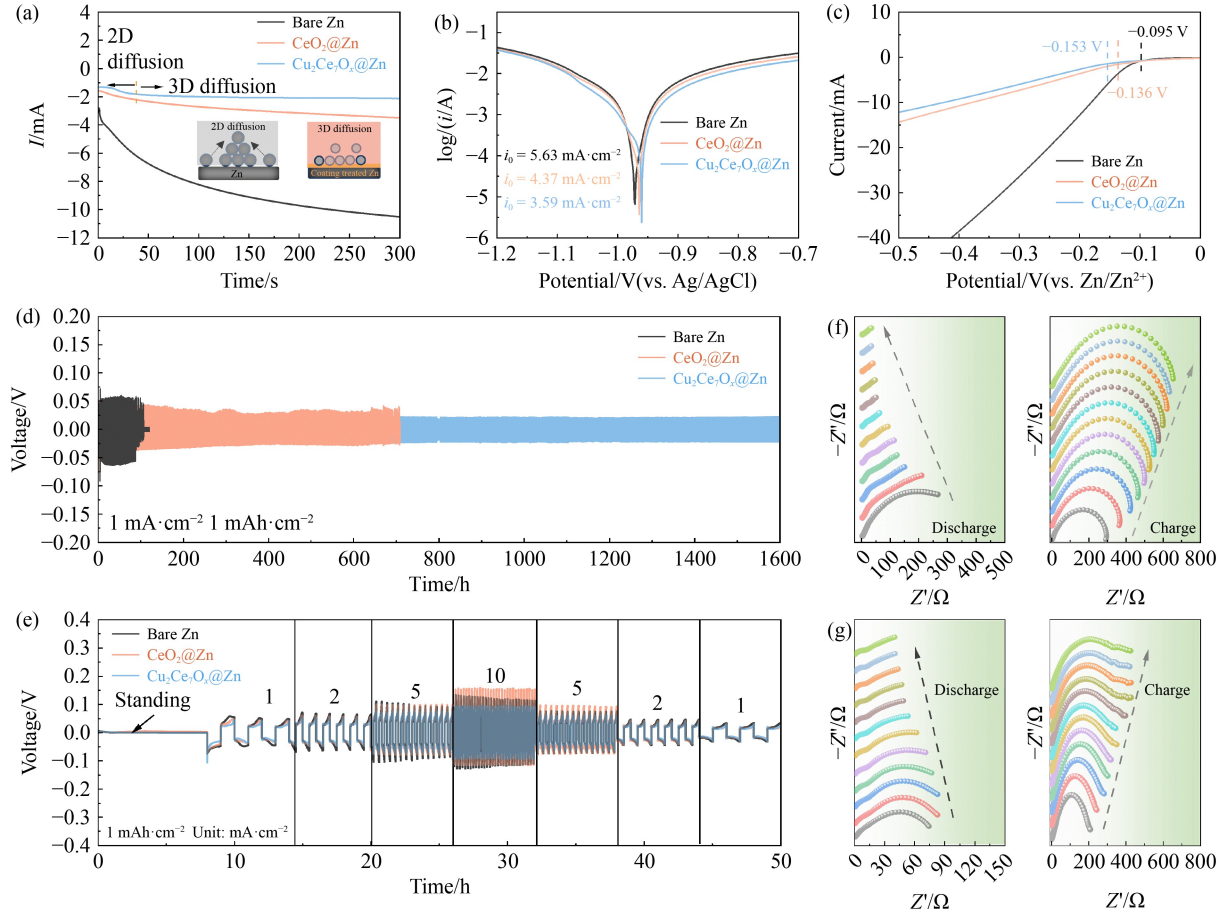

Fig. 5 Electrochemical tests related to the influences on nucleation and Zn deposition.

(a) Chronoamperometric curves; (b) Tafel curves; (c) linear sweep voltammetry (LSV) of symmetric cells with bare Zn, CeO_2@Zn, $Cu_2Ce_7O_x$@Zn; (d) time–voltage curves of symmetric cells under the conditions of (1 mA·cm^{-2})/(1 mAh·cm^{-2}); (e) rate performance of bare Zn/bare Zn, CeO_2@Zn/CeO_2@Zn, and $Cu_2Ce_7O_x$@Zn/$Cu_2Ce_7O_x$@Zn symmetric cells; (f) *in situ* impedance test of bare Zn/bare Zn symmetric cells; (g) *in situ* impedance test of $Cu_2Ce_7O_x$@Zn/$Cu_2Ce_7O_x$@Zn symmetric cells.

CeO_2@Zn and $Cu_2Ce_7O_x$@Zn electrodes showed a different pattern. After 50 s, the current density remains basically stable. This is because CeO_2 and $Cu_2Ce_7O_x$ provide nucleation sites for the electrodes, restricting the migration of Zn^{2+} on the electrode surface. As a result, Zn^{2+} can nucleate and grow uniformly under the action of the electric field. They show a three-dimensional (3D) progressive nucleation mode in the subsequent deposition process [58,59]. This nucleation mode can limit the movement of Zn^{2+} on the CeO_2@Zn and $Cu_2Ce_7O_x$@Zn electrode surface. Moreover, nucleation can occur simultaneously in multiple directions on the CeO_2@Zn and $Cu_2Ce_7O_x$@Zn electrode surface, which is conducive to increasing of nucleation sites and improving the deposition efficiency, thereby inhibiting the formation of dendrites. More importantly, because of the strong adsorption energy of CeO_2@Zn electrode for Zn^{2+}, it is not conducive to the homogeneous deposition of Zn^{2+} in the subsequent deposition process on the CeO_2@Zn electrode surface.

Corrosion resistance and hydrogen evolution: To further investigate of the kinetic processes of the three kinds of Zn electrodes, Tafel curves [60,61] were obtained to characterize the protective effect of artificial layer on Zn anode (Fig. 5(b)), and the corrosion potentials and corrosion currents of the electrodes were measured. The $Cu_2Ce_7O_x$@Zn electrode has the highest corrosion potential and the lowest corrosion current, indicating that it has superior corrosion resistance both thermodynamically and kinetically. Furthermore, LSV was used to examine the hydrogen evolution potentials of bare Zn/bare Zn, CeO_2@Zn/CeO_2@Zn, and $Cu_2Ce_7O_x$@Zn/$Cu_2Ce_7O_x$@Zn symmetric cells, respectively (Fig. 5(c)). Obviously, the hydrogen evolution potential of $Cu_2Ce_7O_x$@Zn/$Cu_2Ce_7O_x$@Zn symmetric cell is more negative than others. $Cu_2Ce_7O_x$@Zn shows outstanding ability in inhibiting the corrosion resistance and hydrogen evolution potential, which is crucial for achieving uniform deposition of Zn^{2+}.

Cyclic stability: To evaluate the long-term stability of the Zn anode, symmetric cells with bare Zn/bare Zn, CeO_2@Zn/CeO_2@Zn, and $Cu_2Ce_7O_x$@Zn/$Cu_2Ce_7O_x$@Zn

electrodes were cycled for a prolonged period (Fig. 5(d)). The bare Zn/bare Zn symmetric cell short-circuited and failed after approximately 90 hours while the CeO_2@Zn/CeO_2@Zn symmetric cell lasted for 700 h. Although CeO_2@Zn electrode can improve cell cycle performance, its overly strong adsorption effect on Zn^{2+} leads to unfavorable Zn desorption/adsorption during deposition. The bare Zn/bare Zn and CeO_2@Zn/CeO_2@Zn symmetric cell display a cyclic stability of 147 and 700 h and an overpotential of 53 and 36 mV. In contrast, the $Cu_2Ce_7O_x$@Zn/$Cu_2Ce_7O_x$@Zn symmetric cell has exceptional stability, cycling for more than 1600 h with an overpotential of only 24 mV. Moreover, the R_{ct} for the $Cu_2Ce_7O_x$@Zn/$Cu_2Ce_7O_x$@Zn symmetric cell is only 150 Ω at room temperature, which is lower than the R_{ct} of the bare Zn/bare Zn (332 Ω) and CeO_2@Zn/CeO_2@Zn (202 Ω) symmetric cells (Fig. S12). These results show that Cu atoms doping changes the physicochemical properties of the CeO_2 substrate, balancing the adsorption energy and migration energy of Zn^{2+}, enhancing the performance of the ZMBs.

High current performance: Even at a high current density of 5 mA/cm^2, the $Cu_2Ce_7O_x$@Zn/$Cu_2Ce_7O_x$@Zn symmetric cell can still cycle for nearly 1600 h, indicating excellent stability under demanding conditions (Fig. S13). Furthermore, rate performance tests reveals that the overpotential for $Cu_2Ce_7O_x$@Zn is the smallest, indicating its excellent interface stability (Fig. 5(e)).

Coulombic efficiency: In the long-cycle test using Cu/Zn asymmetric cells at a current density of 2 mA/cm^2 and a capacity of 1 mAh/cm^2 (Fig. S15), the $Cu_2Ce_7O_x$@Zn electrode can significantly optimize the Zn deposition process and improve the cycle life, showing a high average Coulombic efficiency [62] of 99.9%. The potential capacity curves demonstrate that $Cu_2Ce_7O_x$@Zn/Cu asymmetric cells have a better reversibility and the lowest nucleation overpotential (Fig. S14).

Impedance analysis: Finally, *in situ* impedance measurements were conducted on symmetric cells during charge/discharge process, at a current density of 0.5 mA/cm^2 and a capacity of 0.5 mAh/cm^2 (Figs. 5 (f) and 5(g)). $Cu_2Ce_7O_x$@Zn/$Cu_2Ce_7O_x$@Zn symmetric cell has a smaller R_{ct} during cycling compared to the bare Zn/bare Zn symmetric cell, indicating that the $Cu_2Ce_7O_x$@Zn interface remains more stable throughout the cycle and significantly improves the performance of the Zn anode.

In summary, the incorporation of $Cu_2Ce_7O_x$ into the Zn anode interface significantly improves the electrochemical performance, stability, and lifespan of the ZMB. The $Cu_2Ce_7O_x$@Zn electrode provides superior corrosion resistance, enhances Zn deposition uniformity, reduces dendrite formation, and promotes stable cycling performance even under high current densities. These findings demonstrate that $Cu_2Ce_7O_x$ is a promising material for improving the performance of Zn-based batteries, providing better interface stability and a more efficient Zn deposition process.

The study of full cells [63] with MnO_2 cathodes, synthesized with manganese dioxide (MnO_2) cathode, aimed to explore the improvement of the overall performance of the cell by constructing the $Cu_2Ce_7O_x$ interlayer.

Cyclic voltammetry (CV) analysis: The CV curves of the bare Zn/MnO_2, CeO_2@Zn/MnO_2, and $Cu_2Ce_7O_x$@Zn/MnO_2 full cells in the third cycle, at a scanning rate of 0.5 mV/s (Fig. S16) show that the $Cu_2Ce_7O_x$@Zn/MnO_2 full cell has faster redox kinetics and lower polarization overpotential, compared to the other two configurations. The $Cu_2Ce_7O_x$ interlayer helps balance the adsorption/desorption process and migration of Zn^{2+}, thus improving the overall performance of the cell.

Rate performance: To simulate the overall stability of the cells during operation, the rate performance of the three full cells was tested. The $Cu_2Ce_7O_x$@Zn/MnO_2 full cell operates stably with a capacity of 234.5 mAh/g at a current density of 0.2 A/g. Even at a large current density of 2 A/g, the $Cu_2Ce_7O_x$@Zn/MnO_2 full cell still maintained a capacity of 138.9 mAh/g (Fig. 6(a)). This demonstrates the ability of the $Cu_2Ce_7O_x$ interlayer to maintain stable performance at high current densities, ensuring long-term stability.

Galvanostatic charge-discharge (GCD) curves: The GCD curves (Figs. 6(b) and S17) of the $Cu_2Ce_7O_x$@Zn/MnO_2 full cell shows the highest capacity with the smallest electrode polarization, which is consistent with the CV results. These results further indicate that the $Cu_2Ce_7O_x$@Zn interface effectively reduces polarization and enhances the efficiency of the Zn deposition process.

Self-discharge performance: To assess the self-discharge characteristics of the cells, the CeO_2@Zn/MnO_2 and $Cu_2Ce_7O_x$@Zn/MnO_2 were left standing for 24 h to measure the impact of self-discharge on these full cells after one complete cycle (Fig. 6(c)). The $Cu_2Ce_7O_x$@Zn/MnO_2 full cell retained 98.9% of its initial capacity, which is significantly higher than that of the CeO_2@Zn/MnO_2 full cell (90.4%). This highlights the $Cu_2Ce_7O_x$@Zn/MnO_2 full cell's superior ability to maintain capacity during resting periods, likely due to its enhanced interface stability.

Cycle performance: The cycle performance of these full cells was evaluated at current densities of 0.5 and 1 A/g, respectively (Fig. 6(d) and 6(e)). The CeO_2@Zn/MnO_2 and $Cu_2Ce_7O_x$@Zn/MnO_2 show an upward curve for a certain period, which is the electrochemical activation phenomenon of the cells in the initial stage. The $Cu_2Ce_7O_x$/MnO_2 full cell exhibits an initial capacity of 190.1 mAh/g at 0.5 A/g, and retains 145 mAh/g after more than 500 cycles. At a higher current density of 1 A/g, the $Cu_2Ce_7O_x$/MnO_2 full cell displays an initial capacity of 180.9 mAh/g and a remaining specific capacity of 160.9 mAh/g after 800 cycles. These results

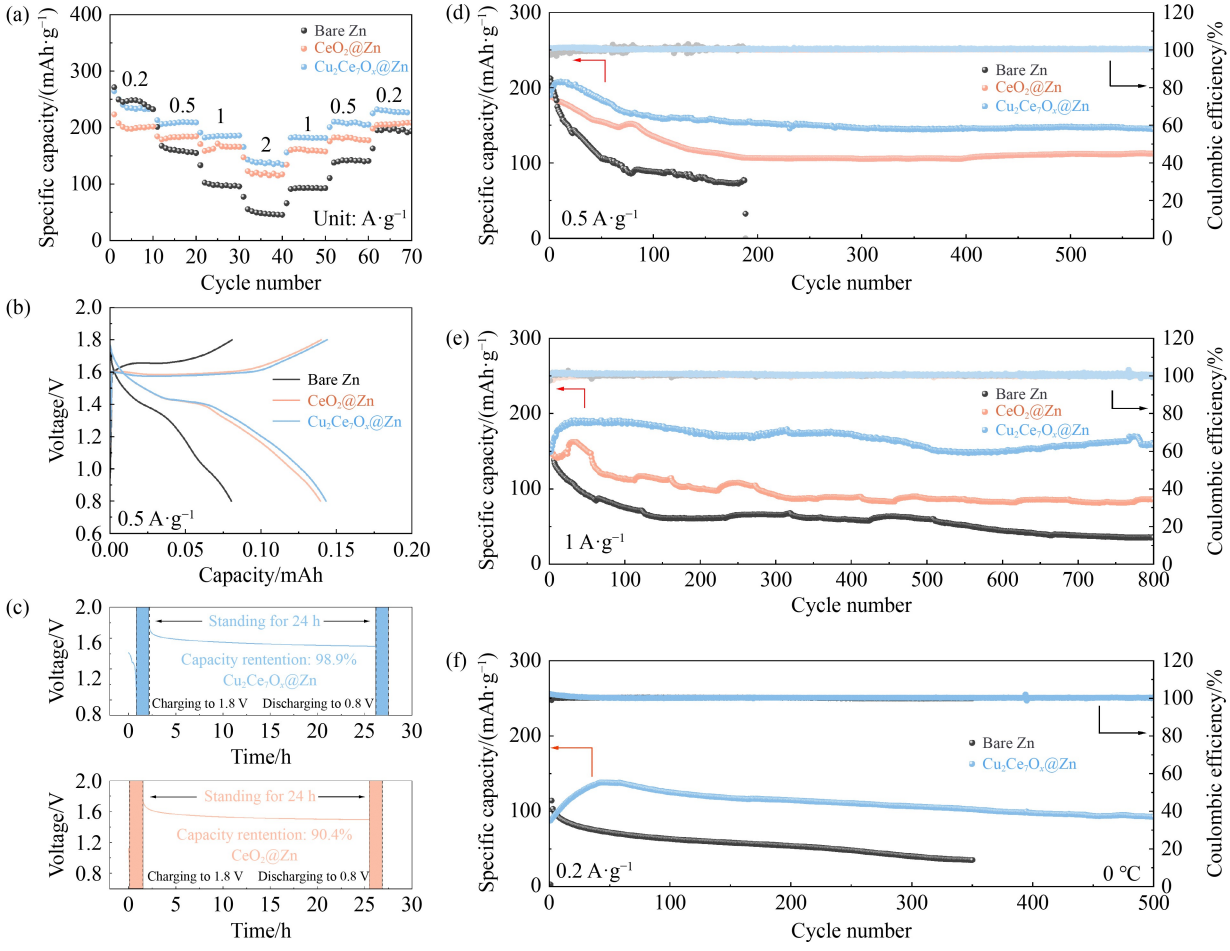

Fig. 6 Comparison of electrochemical performance tests of full cells at different current densities and temperatures. (a) Rate performance; (b) GCD of the full cells with bare Zn/MnO_2, CeO_2@Zn/MnO_2, and $Cu_2Ce_7O_x$@Zn/MnO_2; (c) self-discharge experiments of the full cells with bare Zn/MnO_2, CeO_2@Zn/MnO_2, and $Cu_2Ce_7O_x$@Zn/MnO_2; (d) long cycle tests at current densities of 0.5 A/g; (e) long cycle tests at current densities of 1 A/g; (f) cycle performance test of the full cells with bare Zn/MnO_2 and $Cu_2Ce_7O_x$@Zn/MnO_2 at 0 °C.

indicate that the $Cu_2Ce_7O_x$ artificial interface layer enhances the long-term cycling stability of the Zn-MnO_2 full cells by improving Zn^{2+} migration and deposition, reducing dendrite formation, and maintaining uniform Zn deposition.

Low-temperature performance: To assess the performance of the $Cu_2Ce_7O_x$ interlayer at low temperatures, the cyclic performance of the full cells with bare Zn/MnO_2 and $Cu_2Ce_7O_x$@Zn/MnO_2 was tested at 0 °C. Impressively, the $Cu_2Ce_7O_x$/MnO_2 full cell has a maximum capacity of 138.2 mAh/g at a current density of 0.2 A/g, and the reversible capacity is 92.9 mAh/g after 500 cycles, showcasing its outstanding initial capacity even at subzero temperatures (Fig. 6(f)), which highlights the great potential of the $Cu_2Ce_7O_x$ interlayer to improve the low-temperature stability of ZMBs.

In summary, the $Cu_2Ce_7O_x$ interlayer significantly enhances the performance of Zn/MnO_2 full cells by improving the redox kinetics, reducing polarization, maintaining stable Zn^{2+} migration, and enhancing cycle life. The $Cu_2Ce_7O_x$@Zn/MnO_2 full cell outperforms the bare Zn/MnO_2 and CeO_2@Zn/MnO_2 cells in terms of rate performance, self-discharge retention, and long-term cycling stability. Furthermore, it shows excellent low-temperature performance, demonstrating its great potential for use in practical applications, such as in high-power, long-cycle life, and low-temperature environments. The incorporation of Cu into the CeO_2 matrix effectively balances Zn^{2+} adsorption and migration, making $Cu_2Ce_7O_x$ a promising material for improving the overall performance of Zn-based batteries.

3 Conclusions

In conclusion, this study presents a novel strategy of adjusting the d-band center of CeO_2 and changing the electronic structure by doping Cu metal elements to balance the kinetics of the adsorption/desorption and migration processes of Zn by CeO_2 as interlayers. The

findings indicate that $Cu_2Ce_7O_x$ as the interlayer for Zn anode, provides appropriate adsorption energy and migration energy for Zn^{2+}, which benefits from the regulation of the d-band center.

The $Cu_2Ce_7O_x$ interlayer significantly improves the stability and lifespan of Zn anodes by reducing the overpotential of the Zn^{2+} deposition/stripping process. Electrochemical testing shows that the $Cu_2Ce_7O_x$@Zn electrode maintains a high cycle life of over 1600 h with excellent reversibility and a high average Coulombic efficiency of 99.9% during the deposition/stripping process. Additionally, the $Cu_2Ce_7O_x$@Zn electrode has the smallest initial nucleation overpotential at a current density of 2 mA/cm^2 and a capacity of 1 mAh/cm^2. The $Cu_2Ce_7O_x$@Zn/MnO_2 full cell exhibits remarkable cycling performance, with a capacity retention rate of 92.2% after 800 cycles at a current density 1 A/g, further highlighting the benefits of the $Cu_2Ce_7O_x$ interlayer in enhancing the stability and efficiency of Zn-based batteries.

Overall, this work offers a promising approach to improving Zn anode protection and provides valuable insights for developing advanced strategies to enhance the performance of Zn-MnO_2 full cells and other Zn-based batteries.

Acknowledgements This work was supported by the Fujian Province Super 100 Talents Program; the Pilot Group Program of the Research Fund for International Senior Scientists (No. 22250710676); the National Natural Science Foundation of China (Grant No. 22409029); the Fuzhou University Testing Fund of Precious Apparatus (Nos. 2024T004 and 2024T005), and the Scientific Research Fund for Fuzhou University (Nos. 511336 and 511346).

Competing Interests Jiujun Zhang is the Deputy Editor-in-Chief of Frontiers in Energy, Wei Yan is a member of Editorial Board of Frontiers in Energy who were excluded from the peer-review process and all editorial decisions related to the acceptance and publication of this article. Peer-review was handled independently by the other editors to minimise bias.

Electronic Supplementary Material Supplementary material is available in the online version of this article at https://doi.org/10.1007/s11708-025-1002-8 and is accessible for authorized users.

References

1. Gan L, Liu F, Yuan X, et al. Alumina modified sodium vanadate cathode for aqueous zinc-ion batteries. Frontiers in Energy, 2023, 17(6): 775–781
2. Liu S, Yu X, Yan Y, et al. Dendrite-free lithium deposition enabled by interfacial regulation via dipole-dipole interaction in anode-free lithium metal batteries. Energy Storage Materials, 2023, 62: 102959
3. Zhong Y, Xu X, Veder J P, et al. Self-recovery chemistry and cobalt-catalyzed electrochemical deposition of cathode for boosting performance of aqueous zinc-ion batteries. iScience, 2020, 23(3): 100943
4. Liu J, Xu C, Chen Z, et al. Progress in aqueous rechargeable batteries. Green Energy & Environment, 2018, 3(1): 20–41
5. Liu Y, Lu X, Lai F, et al. Rechargeable aqueous Zn-based energy storage devices. Joule, 2021, 5(11): 2845–2903
6. Ruan P, Liang S, Lu B, et al. Design strategies for high-energy-density aqueous zinc batteries. Angewandte Chemie International Edition, 2022, 61(17): e202200598
7. Li Z, Beyene T T, Zhu K, et al. Realizing fast plating/stripping of high-performance Zn metal anode with a low Zn loading. Journal of Metals, Materials and Minerals, 2024, 34(2): 2009
8. Lenhart B, Kathan D, Hiemer V, et al. Statistical approach to design Zn particle size, shape, and crystallinity for alkaline batteries. Frontiers in Energy, 2024, 18(5): 650–664
9. Liu W, Liu X, Ning F, et al. Fabrication of a heterovalent dual-cation pre-embedded hydrated vanadium oxide cathode for high-performance zinc ion storage. Journal of Materials Chemistry. A, Materials for Energy and Sustainability, 2024, 12(20): 11883–11894
10. Wu K, Liu X, Ning F, et al. Engineering of charge density at the anode/electrolyte interface for long-life Zn anode in aqueous zinc ion battery. ChemSusChem, 2025, 18(1): e202401251
11. Yan Y, Shu C, Zheng R, et al. Modulating sand's time by ion-transport-enhancement toward dendrite-free lithium metal anode. Nano Research, 2022, 15(4): 3150–3160
12. Wang C, Liu S, Xu H, et al. Adjusting Li^+ solvation structures via dipole–dipole interaction to construct inorganic-rich interphase for high-performance Li metal batteries. Small, 2024, 20(24): 2308995
13. Zhang X, Hu J P, Fu N, et al. Comprehensive review on zinc-ion battery anode: Challenges and strategies. InfoMat, 2022, 4(7): e12306
14. Yu X, Li Z, Wu X, et al. Ten concerns of Zn metal anode for rechargeable aqueous zinc batteries. Joule, 2023, 7(6): 1145–1175
15. Yang J, Yin B, Sun Y, et al. Zinc anode for mild aqueous zinc-ion batteries: Challenges, strategies, and perspectives. Nano-Micro Letters, 2022, 14(1): 42
16. Xu Y, Guo Z, Song M, et al. Electrolyte stabilizes Zn^{2+} reduction reaction process: Solvation, interface and kinetics. Batteries & Supercaps, 2024, 7(11): e202400237
17. Yang H, Chen D, Zhao R, et al. Reunderstanding aqueous Zn electrochemistry from interfacial specific adsorption of solvation structures. Energy & Environmental Science, 2023, 16(7): 2910–2923
18. Li B, Liu S, Geng Y, et al. Achieving stable zinc metal anode via polyaniline interface regulation of Zn ion flux and desolvation. Advanced Functional Materials, 2024, 34(5): 2214033
19. Song Y, Huang S, Li C, et al. Regulating solvation structure and enhancing anion-derived solid electrolyte interphase with *N*, *N*′-dimethylpropyleneurea co-solvent for long-term and dendrite-free Zn metal anodes. Energy Storage Materials, 2024, 71: 103629
20. Wang M, Ma J, Meng Y, et al. High-capacity zinc anode with 96 % utilization rate enabled by solvation structure design. Angewandte Chemie International Edition, 2023, 62(3): e202214966
21. Zhang H, Ning F, Guo Y, et al. Unraveling the mechanisms of aqueous zinc ion batteries via first-principles calculations. ACS Energy Letters, 2024, 9(10): 4761–4784

22. You C, Wu R, Yuan X, et al. An inexpensive electrolyte with double-site hydrogen bonding and a regulated Zn^{2+} solvation structure for aqueous Zn-ion batteries capable of high-rate and ultra-long low-temperature operation. Energy & Environmental Science, 2023, 16(11): 5096–5107
23. Meng Q, Bai Q, Zhao R, et al. Attenuating water activity through impeded proton transfer resulting from hydrogen bond enhancement effect for fast and ultra-stable Zn metal anode. Advanced Energy Materials, 2023, 13(44): 2302828
24. Zhan S, Guo Y, Wu K, et al. Regulating the interfacial charge density by constructing a novel Zn anode-electrolyte interface for highly reversible Zn anode. Chemistry, 2024, 30(3): e202303211
25. Feng D, Cao F, Hou L, et al. Immunizing aqueous Zn batteries against dendrite formation and side reactions at various temperatures via electrolyte additives. Small, 2021, 17(42): 2103195
26. Xie C, Li Y, Wang Q, et al. Issues and solutions toward zinc anode in aqueous zinc-ion batteries: A mini review. Carbon Energy, 2020, 2(4): 540–560
27. Shin J, Lee J, Park Y, et al. Aqueous zinc ion batteries: Focus on zinc metal anodes. Chemical Science, 2020, 11(8): 2028–2044
28. Guo N, Huo W, Dong X, et al. A review on 3D zinc anodes for zinc ion batteries. Small Methods, 2022, 6(9): 2200597
29. Li B, Ruan P, Xu X, et al. Covalent organic framework with 3D ordered channel and multi-functional groups endows Zn anode with superior stability. Nano-Micro Letters, 2024, 16(1): 76
30. Cha J S, Park S, Hwang Y, et al. Stable zinc metal battery development: Using fibrous zirconia for rapid surface conduction of zinc ions with modified water solvation structure. Small, 2025, 21(1): 2406481
31. Wang J, Zhang H, Yang L, et al. *In situ* implanting 3D carbon network reinforced zinc composite by powder metallurgy for highly reversible Zn-based battery anodes. Angewandte Chemie International Edition, 2024, 63(10): e202318149
32. Li B, Liu S, Geng Y, et al. Achieving stable zinc metal anode via polyaniline interface regulation of Zn-ion flux and desolvation. Advanced Functional Materials, 2024, 34(5): 2214033
33. Han W, Tan Y, Ni L, et al. Sn penetrated zincophilic interface design in porous Zn substrate for high performance Zn-ion battery. Small Methods, 2024, 2401499
34. Luan X, Qi L, Zheng Z, et al. Step by step induced growth of zinc-metal interface on graphdiyne for aqueous zinc-ion batteries. Angewandte Chemie International Edition, 2023, 62(8): e202215968
35. Zheng S, Zhao W, Chen J, et al. 2D materials boost advanced Zn anodes: Principles, advances, and challenges. Nano-Micro Letters, 2023, 15(1): 46
36. Li C, Xie X, Liang S, et al. Issues and future perspective on zinc metal anode for rechargeable aqueous zinc-ion batteries. Energy & Environmental Materials, 2020, 3(2): 146–159
37. Zong Q, Lv B, Liu C, et al. Dendrite-free and highly stable Zn metal anode with $BaTiO_3$/P(VDF-TrFE) coating. ACS Energy Letters, 2023, 8(7): 2886–2896
38. Zhao C, Zhang Y, Gao J, et al. Zincophilic design and the electrode/electrolyte interface for aqueous zinc-ion batteries: A review. Batteries & Supercaps, 2023, 6(5): e202200478
39. Lee B, Son M G, Song S A, et al. Insights into the design of zincophilic artificial protective layers enabling uniform nucleation and deposition for stable dendrite-free Zn anodes. Journal of Colloid and Interface Science, 2024, 680(Pt B): 640–650
40. Liu J, Ye C, Wu H, et al. 2D mesoporous zincophilic sieve for high-rate sulfur-based aqueous zinc batteries. Journal of the American Chemical Society, 2023, 145(9): 5384–5392
41. Mawintorn T, Lolupiman K, Kiatwisarnkij N, et al. Fabrication and characterization of zinc anode on nickel conductive cloth for high-performance zinc ion battery applications. Journal of Metals, Materials and Minerals, 2024, 34(3): 2083
42. Jin S, Yin J, Gao X, et al. Production of fast-charge Zn-based aqueous batteries via interfacial adsorption of ion-oligomer complexes. Nature Communications, 2022, 13(1): 2283
43. Meng Y, Wang M, Xu J, et al. Balancing interfacial reactions through regulating p-band centers by an indium tin oxide protective layer for stable Zn metal anodes. Angewandte Chemie International Edition, 2023, 62(40): e202308454
44. Zong Q, Li R, Wang J, et al. Tailoring the whole deposition process from hydrated Zn^{2+} to Zn^0 for stable and reversible Zn anode. Angewandte Chemie International Edition, 2024, 63(41): e202409957
45. Wang C, Ouyang T, Wang X, et al. Accelerating lithium ion transport via increasing the entropy of the electrolyte for stable lithium metal batteries. Journal of Energy Chemistry, 2024, 99: 384–392
46. Li Y, Bai X, Yuan D, et al. Cu-based high-entropy two-dimensional oxide as stable and active photothermal catalyst. Nature Communications, 2023, 14(1): 3171
47. Li Y, Yu Z, Huang J, et al. Constructing solid electrolyte interphase for aqueous zinc batteries. Angewandte Chemie International Edition, 2023, 62(47): e202309957
48. Yang J, Zhao R, Wang Y, et al. Insights on artificial interphases of Zn and electrolyte: Protection mechanisms, constructing techniques, applicability, and prospective. Advanced Functional Materials, 2023, 33(14): 2213510
49. Gao F, Tang Y, Liu J, et al. Nickel foam supported cuce mixed metal oxide as monolith catalyst for no removal. Chemical Engineering Journal, 2023, 474: 145713
50. Hou T, Fong K D, Wang J, et al. The solvation structure, transport properties and reduction behavior of carbonate-based electrolytes of lithium-ion batteries. Chemical Science, 2021, 12(44): 14740–14751
51. Wang T, Wang P, Pan L, et al. Stabling zinc metal anode with polydopamine regulation through dual effects of fast desolvation and ion confinement. Advanced Energy Materials, 2023, 13(5): 2203523
52. Yang H, Chang Z, Qiao Y, et al. Constructing a super-saturated electrolyte front surface for stable rechargeable aqueous zinc batteries. Angewandte Chemie International Edition, 2020, 59(24): 9377–9381
53. Yu X, Chen M, Li Z, et al. Unlocking dynamic solvation chemistry and hydrogen evolution mechanism in aqueous zinc batteries. Journal of the American Chemical Society, 2024, 146(25): 17103–17113
54. Dong D, Wang T, Sun Y, et al. Hydrotropic solubilization of zinc

acetates for sustainable aqueous battery electrolytes. Nature Sustainability, 2023, 6(11): 1474–1484

55. Wang C, Liu S, Wang X, et al. Energy level regulation of anions via hydrogen bond effects to construct a stable solid electrolyte interface for a high-stability lithium metal anode. Chemical Communications, 2024, 60(55): 7045–7048
56. Liu X, Guo Y, Ning F, et al. Fundamental understanding of hydrogen evolution reaction on zinc anode surface: A first-principles study. Nano-Micro Letters, 2024, 16(1): 111
57. Yang C, Woottapanit P, Geng S, et al. Highly reversible Zn anode design through oriented ZnO (002) facets. Advanced Materials, 2024, 36(49): 2408908
58. Xie W, Zhu K, Jiang W, et al. Highly 002-oriented dendrite-free anode achieved by enhanced interfacial electrostatic adsorption for aqueous zinc-ion batteries. ACS Nano, 2024, 18(32): 21184–21197
59. Mu Y, Li Z, Wu B, et al. 3D hierarchical graphene matrices enable stable Zn anodes for aqueous Zn batteries. Nature Communications, 2023, 14(1): 4205
60. Li C, Zhang X, Qu G, et al. Highly reversible Zn metal anode securing by functional electrolyte modulation. Advanced Energy Materials, 2024, 14(34): 2400872
61. Guo Q, Mo W, Huang J, et al. Reconfiguring the coordination structure in deep eutectic electrolytes for enabling stable operation of zinc-ion batteries. Nano Letters, 2024, 24(47): 14965–14972
62. Wu Z, Wang Y, Zhi C. Zinc-anode reversibility and capacity inflection as an evaluation criterion. Joule, 2024, 8(9): 2442–2448
63. Lolupima K, Cao J, Zhang D, et al. A review on the development of metals-doped vanadium oxides for zinc-ion battery. Journal of Metals, Materials and Minerals, 2024, 34(3): 2084